

## BIOPHYSICS

# Hyaluronan orders water molecules in its nanoscale extended hydration shells

J. Dedic<sup>1\*</sup>, H. I. Okur<sup>1,2\*</sup>, S. Roke<sup>1†</sup>

**Hyaluronan (HA) is an anionic, highly hydrated bio-polyelectrolyte found in the extracellular environment, like the synovial fluid between joints. We explore the extended hydration shell structure of HA in water using femto-second elastic second-harmonic scattering (fs-ESHS). HA enhances orientational water-water correlations. Angle-resolved fs-ESHS measurements and nonlinear optical modeling show that HA behaves like a flexible chain surrounded by extended shells of orientationally correlated water. We describe several ways to determine the concentration-dependent size and shape of a polyelectrolyte in water, using the amount of water oriented by the polyelectrolyte charges as a contrast agent. The spatial extent of the hydration shell is determined via temperature-dependent measurements and can reach up to 475 nm, corresponding to a length of 1600 water molecules. A strong isotope effect, stemming from nuclear quantum effects, is observed when light water (H<sub>2</sub>O) is replaced by heavy water (D<sub>2</sub>O), amounting to a factor of 4.3 in the scattered SH intensity.**

## INTRODUCTION

Water has a key function in biology as it is the primary solvent of life. It actively participates in biochemical transformations such as protein folding, molecular recognition, self-assembly, and joint lubrication (1–4). To elucidate the role that various constituents of the body play in sustaining life, it is important to take into account their interaction with the aqueous environment. One example where water plays a very important role is in the extracellular matrix of epithelial and connective tissues. The matrix is rich in hyaluronan (HA), an anionic poly-disaccharide composed of D-N-acetylglucosamine and D-glucuronic acid (displayed in Fig. 1A) (5). HA has the ability to retain up to 10× its dry weight of water (6–11) and creates a gel-like pericellular coat (12, 13). HA is a component in nearly every part of the body, varying in concentration from 10 ng/ml (~12 pM) to ~3 mg/ml (3.5 μM) (5), and its hydration is thought to be key for the functioning of moving joints (12, 14, 15). HA has been studied in solution with linear light (16) and neutron scattering (16, 17) at concentrations above 100 μg/ml, with mid-sized (tens to thousands of kilodaltons) macromolecules. At concentrations <100 μg/ml (<~0.1 μM), the size and shape of the polyelectrolyte are unknown. Several theoretical models (18–20) exist for predicting the shape of polyelectrolytes, taking into account both thermal motion and electrostatics; however, these are only partially valid because they require rigid macromolecules (such as DNA), a condition that is not met for HA. Calorimetric (21, 22), vibrational spectroscopic (23–25), and compressibility (26) studies indicate slower hydrogen (H)–bonding dynamics and different thermodynamic properties of the hydrating water compared to bulk water. However, the observed effects of HA are limited to the first or second hydration shell. Recent developments in nonlinear optical spectroscopy allow direct probing of the orientational order in the H-bonding network of water over nanoscale distances and under extreme dilution (27).

This enables further investigation of HA hydration under more dilute conditions, exploring weaker and longer-ranged interactions.

The structure of water near ions and charged groups is perturbed relative to neat water due to well-known ion-dipole and H-bonding interactions (28–30). However, the spatial extent over which ions perturb the structure of water is still a subject of debate (27, 31–33). Ions are traditionally assumed to have a short-range ordering effect, influencing the structure of, at most, the first three layers of hydrating water. This notion is supported by dielectric and terahertz spectroscopy (34, 35), x-ray (36) and neutron scattering (37), vibrational spectroscopies (38–40), and computational simulations (41, 42). However, recent studies based on femtosecond elastic second-harmonic scattering (fs-ESHS) experiments (27, 43, 44), supported by computational studies (45, 46), are changing this long-held notion that ion-water interactions are limited to several angstroms. Unlike most experimental techniques, which are often inherently limited to subnanometer length scales or equivalently require >100 mM solute concentrations, fs-ESHS directly probes spatial correlations over length scales comparable to the wavelength of the light used and in very dilute solutions (47). Using fs-ESHS, a nonspecific long-range (~20 nm) influence of simple electrolyte ions on the hydrogen (H)–bonding network of water molecules was found that starts at ionic strengths as low as 10 μM (27). This observation was explained as an electric field–induced perturbation in the water-water orientational correlations. Moreover, there is a noticeable nuclear quantum effect that is yet to be explained.

Here, we measure the orientational order of water in HA solutions and explore the extended hydration shell structure of HA in light and heavy water using fs-ESHS. We observe that water-water orientational correlations are enhanced by HA substantially more than by simple salts. The increased order in water is measurable from HA concentrations ranging from <1 pM up to ~1 μM, with an excess ionic strength range from 1 nM to 10 mM. A substantial isotope effect is observed when light water (H<sub>2</sub>O) is replaced by heavy water (D<sub>2</sub>O). The onset concentration increases in D<sub>2</sub>O by a factor of 2.4, and the scattered intensity is 4.3× lower than in H<sub>2</sub>O. Angle-resolved fs-ESHS measurements were performed to investigate the structure and size of water-HA complexes. Using nonlinear light scattering theory to model the intensity generated by the oriented

<sup>1</sup>Laboratory for Fundamental BioPhotonics (LBP), Institute of Bioengineering (IBI), and Institute of Materials Science (IMX), School of Engineering (STI), and Lausanne Centre for Ultrafast Science (LACUS), École Polytechnique Fédérale de Lausanne (EPFL), CH-1015 Lausanne, Switzerland. <sup>2</sup>Department of Chemistry and National Nanotechnology Research Center (UNAM), Bilkent University, 06800 Ankara, Turkey.

\*These authors contributed equally to this work.

†Corresponding author. Email: sylvie.roke@epfl.ch

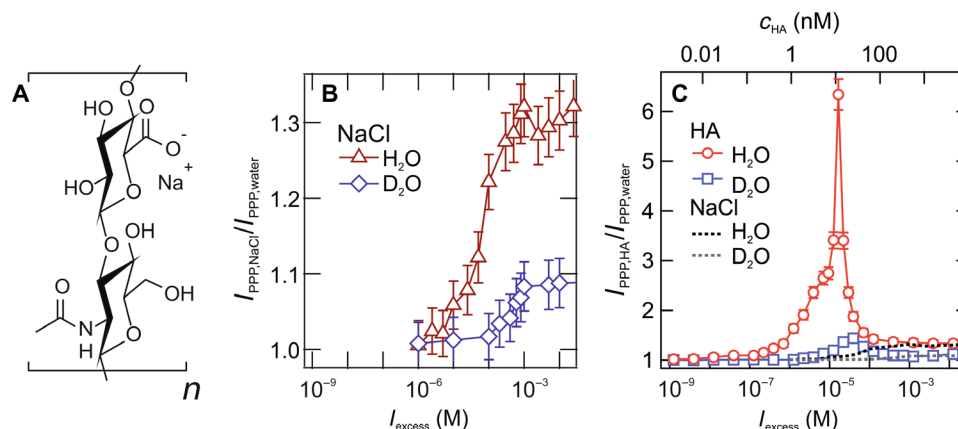


**Fig. 1. HA enhances orientational correlations between water molecules.** (A) Molecular structure of HA, where each disaccharide monomer has one negatively charged carboxylate group. (B) Normalized fs-ESHS intensity as a function of ionic strength for NaCl dissolved in light ( $\text{H}_2\text{O}$ ) and heavy ( $\text{D}_2\text{O}$ ) water obtained with all beams polarized along the horizontal plane (PPP polarization combination). (C) Normalized fs-ESHS intensity as a function of excess ionic strength (and concentration of HA) for HA (molecular weight, 1145 kDa) dissolved in light ( $\text{H}_2\text{O}$ ) and heavy ( $\text{D}_2\text{O}$ ) water obtained in PPP polarization combination. Note that  $I_{\text{excess}}$  only includes the ions coming from the polyelectrolyte. The dotted lines represent the data for NaCl in (B). The relative intensity maximum  $I_{\text{PPP}(\text{CHA})}/I_{\text{PPP, water}} = 6.3$  at a  $c_{\text{CHA}} = 11.6$  nM (13.3  $\mu\text{g}/\text{ml}$ ,  $I_{\text{excess}} = 6.3$   $\mu\text{M}$ ) for  $\text{H}_2\text{O}$  and  $I_{\text{PPP}(\text{CHA})}/I_{\text{PPP, water}} = 1.45$  at a  $c_{\text{CHA}} = 27$  nM (32  $\mu\text{g}/\text{ml}$ ,  $I_{\text{excess}} = 39.5$   $\mu\text{M}$ ) for  $\text{D}_2\text{O}$ .

water, two different spherical radii are determined,  $R$  and  $R'$ .  $R$  is the size of an on average spherical object where the electrostatic potential has a maximum. At  $R'$ , this electrostatic potential has decayed to 2% of its maximum value. Temperature-dependent angle-resolved fs-ESHS measurements were performed to determine the size of the extended hydration shell at the concentration of maximum fs-ESHS intensity. The extended hydration shell ( $R_h$ ) is determined by the water that is associated directly with the HA chain by molecular interactions, and  $R < R_h < R'$ . The extended spherical hydration shell  $R_h$  that includes the HA macromolecule spans up to 475 nm in  $\text{H}_2\text{O}$  and 260 nm in  $\text{D}_2\text{O}$ , corresponding to a line of 1600 (928) water molecules in  $\text{H}_2\text{O}$  ( $\text{D}_2\text{O}$ ).

## RESULTS AND DISCUSSION

### fs-ESHS from HA in $\text{H}_2\text{O}$ and $\text{D}_2\text{O}$

To provide context, we first recount a recent finding concerning fs-ESHS measurements performed on aqueous solutions of simple electrolytes. Figure 1B shows the fs-ESHS intensity recorded at a scattering angle  $\theta$  of  $90^\circ$  for NaCl in  $\text{H}_2\text{O}$  (red triangles) and  $\text{D}_2\text{O}$  (tilted blue squares). The data were adapted from (27, 48). The increase in the fs-ESHS intensity was attributed to arise from an increase in the orientational order in the H-bonding network of water due to the interaction of the ionic electrostatic field with the H-bonded network. The intensity starts increasing from a salt concentration of  $\sim 10$   $\mu\text{M}$  and saturates at  $\sim 1$  mM. Electrolytes dissolved in  $\text{D}_2\text{O}$  show the same trend as in  $\text{H}_2\text{O}$  but with a  $\sim 6\times$  higher onset concentration and a 36% smaller saturation value, relative to the pure  $\text{H}_2\text{O}$  or  $\text{D}_2\text{O}$  solvent. This slight restructuring of the H-bonding network also manifests itself on the macroscopic length scale as the Jones-Ray effect (32), an anomalous decrease of the surface tension at the fs-ESHS saturation concentrations. The increase in orientational order in the bulk solution gives rise to an entropic penalty, which reduces the surface tension (27, 32, 49).

Figure 1C shows fs-ESHS data obtained in the same manner for HA (molecular weight, 1145 kDa) dissolved in  $\text{H}_2\text{O}$  (red circles) and  $\text{D}_2\text{O}$  (blue squares) plotted as a function of calculated excess

ionic strength and HA concentration in nM. fs-ESHS is a nonresonant process in which each molecular group contributes a comparable amount to the total nonlinear polarization in the solution. The intensity that is measured scales with the absolute square of the nonlinear polarization. At an HA concentration of 11.6 nM (13.3  $\mu\text{g}/\text{ml}$ ), the relative amount of HA monomers to  $\text{H}_2\text{O}$  molecules is  $\sim 13 \times 10^{-6}$ , which means that the intensity ratio of  $\text{H}_2\text{O}:\text{HA}$  is  $\sim 10^{10}$ . The fs-ESHS technique therefore reports on the water structure and not on the HA structure. Measuring the coherent part of the intensity, one obtains information about the strength of water-water correlations and, therefore, the H-bonding network of water. The total ionic strength ( $I$ ) in the solution is given by  $I = I_0 + I_{\text{excess}}$ , where  $I_0$  is the ionic strength of an infinitely dilute solution (which includes the auto-ionization of the water), and  $I_{\text{excess}} = c_{\text{HA, mon.}}/2$ , the excess ionic strength with  $c_{\text{HA, mon.}}$ , the concentration of HA monomers. The fs-ESHS data were recorded in the same way as the data in Fig. 1B, at a scattering angle  $\theta$  of  $90^\circ$  and with all beams P-polarized, i.e., oscillating in the horizontal scattering plane. Further information about the experiment is given in Materials and Methods and figs. S1 and S2 that provide SH power dependence and spectroscopic data. The fs-ESHS intensity of HA solutions at ionic strengths below 10 mM is much larger than that of simple electrolyte solutions, reaching  $\sim 6.3\times$  the response of bulk water for  $\text{H}_2\text{O}$  and  $\sim 1.4\times$  the response of bulk  $\text{D}_2\text{O}$ . The intensity increase also occurs at exceptionally low HA concentrations: At  $c_{\text{HA}} \sim 30$  pM ( $I_{\text{excess}} \sim 10^{-8}$  M), the intensity increases beyond that of NaCl and reaches a maximum at  $c_{\text{HA}} = 11.6$  nM ( $I_{\text{excess}} = 6.3$   $\mu\text{M}$ ) for HA in  $\text{H}_2\text{O}$ . For HA in  $\text{D}_2\text{O}$ , the intensity increases at  $c_{\text{HA}} \sim 1$  nM ( $I_{\text{excess}} \sim 10^{-6}$  M) and reaches a maximum at  $c_{\text{HA}} \sim 27$  nM ( $I_{\text{excess}} \sim 39.5$   $\mu\text{M}$ ). The intensity plateau reached above 1 mM for  $\text{H}_2\text{O}$  and 10 mM for  $\text{D}_2\text{O}$  is the same for HA and NaCl in their respective solvents. Note that these HA concentrations are far below those probed previously with other techniques [ $>100$   $\mu\text{g}/\text{ml}$ , and 117 nM only in  $\text{H}_2\text{O}$ ; (16, 17, 20) and summarized in table S1].

The increased magnitude of the fs-ESHS intensity shows that the amount of orientational order in the water as induced by HA is much greater for HA compared to NaCl. This indicates that the

interaction of the electrostatic field from the ionic groups on the HA polymers with the H-bonding network in water is much stronger than the same type of interaction in the electrolyte solution. This is caused by the spatial arrangement of the ionic groups on the polymer: Each HA monomer, 1.02 nm in size, contains one negative charge (Fig. 1A) so that HA has a linear charge density of  $\sim 1 e^-/\text{nm}$  with the entire chain containing  $>3000$  units. As the spacing of charges is larger than the Bjerrum length of water (0.71 nm), the ionic groups of HA are ionized. The combination of electrostatic and thermal interactions significantly complicates the description of HA polyelectrolyte structure, and although several models exist (16, 18–20), the structure of HA in solution is unknown in the concentration range of our investigation. It is clear, however, that unlike ions of simple salts, which are statistically distributed in solution, the charges on HA cannot move freely as they are fixed by the polymer chain that links them. These charges are therefore spatially correlated over a certain distance due to the covalent bonding between individual monomers on a single polymer chain and the limited degrees of freedom that the chain has due to bending, thermal motion. In addition, intrachain electrostatic repulsion further limits the flexibility and spatial positioning of the HA chains (19). The concentration of such a large number of electric charges in a small region of space generates much stronger localized electrostatic fields than statistically distributed free ions. This leads to a much stronger effect of the electrostatic field on the H-bonding network of water and thus a much larger fs-ESHS response of HA compared to NaCl.

### Nuclear quantum effects

As can be seen in Fig. 1C, the fs-ESHS response of HA in H<sub>2</sub>O and D<sub>2</sub>O is remarkably different. The fact that replacing light with heavy water in HA solutions significantly alters the fs-ESHS response indicates that the HA chains do not simply order water molecules via a charge-dipole interaction: Charge-dipole interactions would not be detectably affected by a change in the isotope of the water as both water isotopes have nearly identical dielectric constants and dipole moments (50). The isotope effect in the fs-ESHS response points to a more complex process in which the two primary and orthogonal

degrees of freedom to break and form hydrogen bonds, H-bond stretching and H-bond rotation (or libration), are decoupled. The magnitude of the difference further points toward long-range interactions involving many water molecules. In addition, this nuclear quantum effect involves the electric field of HA interacting with the total H-bonding network of water, changing the orientational water-water correlations in the solution (27, 48). Compared to simple electrolytes, HA induces these effects at much lower concentrations [10  $\mu\text{M}$  versus  $\sim 10$  pM of HA ( $I_{\text{excess}} = 10^{-8}$  M for H<sub>2</sub>O) and 100  $\mu\text{M}$  versus  $\sim 1$  nM of HA ( $I_{\text{excess}} = 10^{-6}$  for D<sub>2</sub>O)] and with a much higher magnitude (1.05 versus 6.4 for H<sub>2</sub>O and 1.0 versus 1.4 for D<sub>2</sub>O, at the same ionic strength). Because a similar effect coincides with a small but significant change in a macroscopic property of the solution for simple salts, the much bigger change here might lead to much bigger changes in macroscopic properties of hydrated polyelectrolytes. One such candidate is the viscosity of the liquid (51), which depends on the reorientation of water, and has been correlated to the coherent fs-ESHS response of concentrated aqueous electrolyte solutions (52). Although it is very clear from the experiment what the parameters for describing this nuclear quantum effect should be, up until now, theoretical modeling has not yet been able to capture this behavior (27, 51). To describe the phenomenon observed in Fig. 2 (B and C), it will be necessary to describe HA and its extended surrounding water molecules on a quantum chemistry level. Although these computations have been done on a single water molecule embedded in an environment that can be described by a classical force field (53), the need to do this for a much bigger cluster involving HA and many waters would involve computations on a scale that is currently not feasible. Therefore, in what follows, we revert to classical nonlinear light scattering theory (54, 55) to model the structure of HA polyelectrolyte hydration in H<sub>2</sub>O. We will, therefore, describe angle-resolved and temperature-dependent second-harmonic scattering data of HA in H<sub>2</sub>O and extract relevant length scales that we will then compare with what is known about the conformation of HA (18, 19), thereby adding structural information of HA and its hydration in a range that is currently inaccessible by other methods.

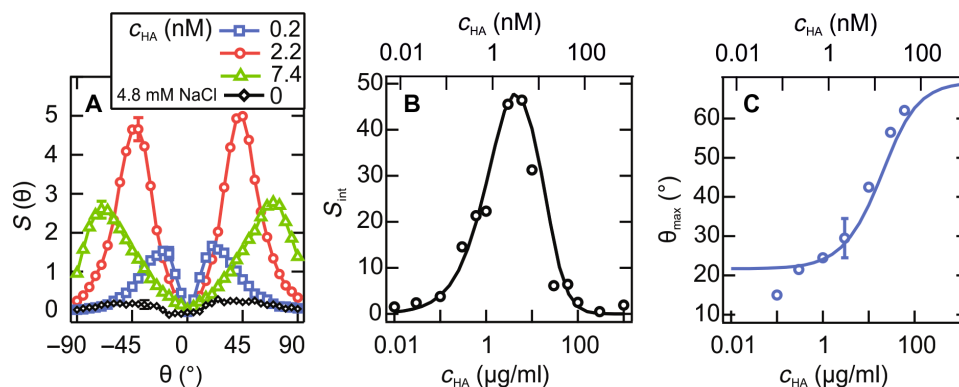


**Fig. 2. Scattering patterns of HA solutions are concentration dependent.** (A) Angle-resolved fs-ESHS measurements of HA solutions (molecular weight, 1349 kDa) in H<sub>2</sub>O measured at three concentrations showing a strong concentration dependence of the angular distribution of the scattered SH light. More concentrated HA solutions scatter at higher angles. 0\* corresponds to a 4.8 mM NaCl solution. The excess ionic strengths of the other solutions are 0.4  $\mu\text{M}$  (0.3  $\mu\text{g/ml}$ ), 3.8  $\mu\text{M}$  (3  $\mu\text{g/ml}$ ), and 12.5  $\mu\text{M}$  (10  $\mu\text{g/ml}$ ). More patterns are shown in the Supplementary Materials (fig. S1). (B) Integrated fs-ESHS intensity as a function of HA concentration. The solid curve shows the predicted behavior based on the proposed model of fs-ESHS and is calculated using Eq. 3. (C) Angle of maximum intensity plotted as a function of HA concentration. The scattering angle at maximum intensity ( $\theta_{\text{max}}$ ) shifts to higher angles with increasing concentration, which is equivalent to scattering from smaller objects. The solid lines were calculated using Eq. 4. The parameters used for the modeling are as follows:  $R = 5\kappa^{-1}$  and  $I_0 = 5 \mu\text{M}$  (see Materials and Methods). The experimental data were measured in the PPP polarization combination. The error bar is representative for all data points.

### Angle-resolved fs-ESHS

To characterize the flexible structure of hydrated HA, we measured angle-resolved fs-ESHS in the entire forward half-plane (from  $\theta = -90^\circ$  to  $\theta = +90^\circ$ ) for HA dissolved in  $H_2O$ . In contrast to single-angle measurements, the angle-resolved measurements provide information about the shape of the emitted scattered light pattern, which is important for further analysis. Three representative angle-resolved scattering patterns of HA solutions at concentrations of 0.2, 2.2, and 7.4 nM (0.3, 3, and 10  $\mu\text{g/ml}$ , with an excess ionic strength of 0.4, 3.8, and 12.5  $\mu\text{M}$ ) and one pattern of a NaCl solution (4.8 mM) are shown in Fig. 2A. Patterns for all of the measured HA concentrations are shown in fig. S3, showing NaCl patterns (fig. S3A) and HA patterns (fig. S3B). The patterns were recorded with all beams polarized along the horizontal scattering plane (PPP polarization combination). The shape of the scattering pattern of a NaCl solution does not vary with salt concentration, as can be seen in fig. S3A. In contrast, the shape and intensity of the HA patterns substantially change with increasing HA concentration. The variations in the data of Fig. 2A can be captured by two key parameters: The integrated fs-ESHS intensity  $S_{\text{int}}$ , calculated by integrating the scattering patterns in the forward half-plane, is shown in Fig. 2B. The angle of maximum scattering intensity  $\theta_{\text{max}}$  is shown in Fig. 2C. Both metrics are illustrated in more detail in fig. S3C.  $S_{\text{int}}$  increases with HA concentration up to  $\sim 5 \mu\text{g/ml}$  (6.25  $\mu\text{M}$ ) and then drops and levels off, very similar to the data measured at  $\theta = 90^\circ$  (Fig. 1B).  $\theta_{\text{max}}$  shifts monotonously from  $\theta_{\text{max}} = 18^\circ$  to  $\theta_{\text{max}} = 65^\circ$  with increasing HA concentration. To understand the unusual concentration dependence, we model the two essential properties of the scattering by using nonlinear light scattering theory. The solid lines in Fig. 2 (B and C) correspond to the result of this model, which we describe next.

### Modeling of the fs-ESHS scattering patterns

Nonlinear light scattering theory has been developed for a variety of systems, including SHS from an isotropic distribution of molecules (56), used to describe the incoherent hyper-Rayleigh scattering from liquids (27, 44, 52), and coherent SHS from spherical surfaces or infinitely thin shells around isotropic particles in an isotropic solution (57–60). HA molecules in solution are macromolecular and have a size range well over a nanometer so that hydrated HA can be thought of as an on-average soft particle. Our measurements report on many such macromolecules in the laser beam focus (with a beam waist of 35  $\mu\text{m}$ ,  $\sim 4.7 \times 10^5$  HA molecules at 11.6 nM) in combination with  $\sim 2.2 \times 10^{11}$  water molecules. The nonresonant SH polarizability reports on every noncentrosymmetric molecule with an equal magnitude (61), and therefore, the SH intensity reports on the water. This means that the coherent water signal determines the nonlinear optical response of our experiment. Furthermore, the averaged water response is influenced by the electrostatic field on the water orientation. It is therefore possible to approach this modeling either by using a model that treats water as a dipolar liquid (27), performs averaging of the hyperpolarizability tensors  $\beta^{(2)}$  and  $\beta^{(3)}$ , and removes the incoherent part or by directly using the coherent part through the susceptibility tensors  $\chi^{(2)}$  and  $\chi^{(3)}$  already available from the nonlinear light scattering theory of spherical objects in solution (47). Although the choice is eventually arbitrary, we use the latter one, applying the Rayleigh-Gans-Debye (RGD) approximation, in which the refractive index contrast between a particle with radius  $R$  and the medium is small (62). We will first

describe the model as it is known and then adjust it to describe the current system. The coherent response is characterized by a second-order surface susceptibility  $\chi_s^{(2)}$ , which captures interfacial chemical interactions. Later models have included the effect of a nonzero surface potential  $\Phi_0$  and ionic strength (via  $\kappa^{-1}$ ) (63). The electrostatic potential decays to  $\sim 2\%$  of its surface value at  $R'$  over a distance of  $4\kappa^{-1}$ ; thus,  $R' = R + 4\kappa^{-1}$  (54). This introduces an effective third-order susceptibility  $\chi^{(3)'}$ , which takes into account the contribution to the coherent SH response of water molecules that are oriented by an electrostatic field. For the present nonresonant excitation,  $\chi^{(3)'}$  has only a single value,  $\chi^{(3)'} = 10.3 \times 10^{-22} \text{ m}^2/\text{V}^2$  (64). Figure 3A shows an illustration of the relevant size parameters in this model. The dimensions  $R$  and  $R'$  are determined by the electrostatic potential ( $\Phi$ ):  $R$  is the radial distance from where the electrostatic potential  $\Phi$  starts to decay into the solution, and  $R'$  is the radial distance where this potential has decayed to 2% of its maximum value, the surface potential,  $\Phi_0$ . For SHS from solid particles, droplets, and liposomes,  $R$  is comparable to the linear light scattering or hydrodynamic radius (62, 64–67). The reason for this is that the refractive index and the electrostatic potential experience discontinuities at approximately the same radial distance. Section S3 contains a more detailed description of RGD SHS from a sphere, which results in the following type of expression for the scattered SH response  $S(\theta)$  in terms of the intensity scattered by a particle dispersion in PPP polarization  $I(\theta)_{\text{PPP, disp}}$ , normalized by the intensity scattered by pure water in the SSS polarization combination  $I(\theta)_{\text{SSS, H}_2\text{O}}$

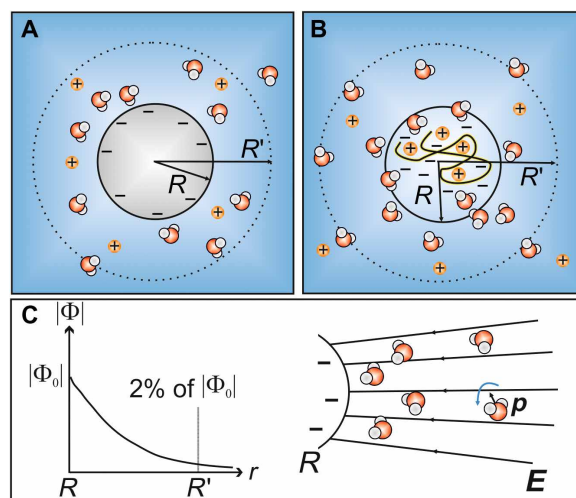


**Fig. 3. Illustration of the model.** (A) Model of nonlinear light scattering from a charged sphere. The source of the SHS signal is water molecules whose orientational distribution is distorted by their interaction with the surface of the particle, as well as water molecules within the dashed circles that are perturbed by the electrostatic field of the particle. (B) Model for scattering from an HA solution. There is no surface, but the electrostatic field of the polymer distorts the orientational distribution of water molecules, leading to SH generation. (C) Illustration of the decay of the electrostatic potential into the aqueous solution (left) and SHS contrast mechanism (right). The arrow labeled “p” indicates the dipole moment of water, which experiences a force from the electrostatic field that emanates from the overall negative charge on the HA chain. This interaction is indicated with the curved blue arrow.  $R$  is the size of the spherical object from which the electrostatic potential starts to decay into the solution.  $R$  is modeled as  $R = \alpha\kappa^{-1}$ . At  $R'$ , only 2% of the electrostatic field is left, and thus,  $R' = R + 4\kappa^{-1}$ .

$$S(\theta) = \frac{I(\theta)_{\text{PPP,disp}}}{I(\theta)_{\text{SSS,H}_2\text{O}}} = N_p |F(q, R, \kappa, \chi_s^{(2)}, \chi^{(3)'}, \Phi_0)|^2 \quad (1)$$

The single-particle response for noninteracting particles, determined by the form factor  $F(q, R, \kappa, \chi_s^{(2)}, \chi^{(3)'}, \Phi_0)$ , is multiplied by the particle density  $N_p$ .  $q$  is the magnitude of the scattering wave vector  $\mathbf{q}$  defined as the difference between the wave vectors of the scattered SH wave vector and the sum of the two fundamental wave vectors.  $q = 4\pi n \sin(\theta/2)/\lambda$ , where  $n$  is the refractive index of the solvent and  $\lambda$  is the SH wavelength. SHS scattering from isotropic particles with isotropic surfaces is characterized by four nonzero polarization combinations (SPS, PSS, PPP, and PSS), four vanishing polarization combinations (SSS, SPP, PPS, and PSP), and the absence of scattered light in the forward direction ( $\theta = 0^\circ$ ) for the four nonvanishing ones. This leads to a characteristic two-lobe pattern, similar to those plotted in Fig. 2A (54, 58, 62, 65). Within this model, the position of the lobes (represented by  $\theta_{\text{max}}$ ) shifts to higher angles with decreasing particle radius. For example, taking a wavelength of 1000 nm, and  $\chi_{s,2}^{(2)} = 1$ , results in  $\theta_{\text{max}} > 50^\circ$  for  $R = 50$  nm, while  $\theta_{\text{max}} < 20^\circ$  is reached when  $R = 500$  nm.

Having described this model, we first consider its applicability to polyelectrolytes in solution and then describe the implemented changes. Figure 2A and fig. S3B show fs-ESHS scattering patterns for HA in the PPP polarization combination, and fig. S4 shows an SSS pattern for HA solutions. These scattering patterns display the same marked features of coherent SH scattering from a particle immersed in water as described above, and so RGD nonlinear light scattering from a sphere embedded in water can be taken as a starting point to describe the data in Fig. 2 (B and C) with the aim to extract relevant length scale information from it. We modify the model based on the differences between HA polymers in solution and a dilute dispersion of noninteracting spherical particles, and add a structure factor to model interactions between the macromolecules. Figure 3B shows an illustration of the changes and assumptions. Figure 3C illustrates the contrast mechanism. First, HA polymers are either folded or stretched and do not have a different medium inside them as is the case for particles or droplets. However, we can still consider the boundary of a polymer as a very porous closed shell with a certain radius  $R$ , as we are measuring many such macromolecules (in the laser focus  $\sim 4.7 \times 10^5$  at 11.6 nM), and the averaged shape of the orientationally ordered water becomes radial.  $R$  can, therefore, be considered as the average effective size of the sphere that encapsulates the folded negatively charged polyelectrolyte chain together with its hydrating water. Within  $R$ , there are polyelectrolyte charges and counter ions that together generate an electrostatic field at radius  $R$ . Outside this radius  $R$ , there are counter ions that are more mobile and result in a slowly decaying electrostatic field, with the Debye ( $1/\kappa$ ) length a determining factor (Fig. 3C). It is the water that is oriented by the electrostatic field in the solutions that is responsible for the ESHS intensity. The Debye length  $\kappa^{-1}$  is given by  $\kappa^{-1} = \sqrt{\frac{\epsilon_0 \epsilon k_B T}{2 \times 10^3 N_A e^2 I}}$ , where  $I$  is the ionic strength in moles per liter,  $T$  is the temperature (298 K),  $e$  is the elementary electric charge,  $k_B$  is the Boltzmann constant,  $N_A$  is Avogadro's number,  $\epsilon_0$  is the vacuum permittivity, and  $\epsilon$  is the dielectric constant of water (78.5). Because the SHS intensity of a single object scales with  $R^6$  (58), the aqueous volume outside of the soft sphere of the polymer chain with radius  $R$  will provide dominant contribution to the SHS intensity. Since this apparent boundary is charged, there will be an electrostatic field that penetrates into the adjacent

extended hydration shell, where it will increase the orientational order of the water. This decay length, taken from the center of the object and indicated by  $R'$ , is  $R' = R + 4\kappa^{-1}$ . Furthermore, as mentioned, because HA has a charge spacing of 1.02 nm, larger than the Bjerrum length in water (0.71 nm), counter-ion condensation will not occur when the HA concentration ( $c_{\text{HA}}$ ) is varied (68). Consequently, the surface potential  $\Phi_0$  can be considered as concentration independent. For dilute solutions, the Debye length spans hundreds of hydration shells: For an ionic strength range of  $\sim 5 \times 10^{-6}$  M (water with no excess ions, in our experiment) to  $\sim 4 \times 10^{-5}$  M (the maximum for HA in H<sub>2</sub>O in Fig. 1C), the Debye length changes from 137 to 45 nm. The distance  $4\kappa^{-1}$  changes from 548 to 180 nm. With the  $I \sim R^6$  scaling in mind, the long-range electrostatic field interaction dominates over the short-range chemical interactions between water and the HA chain. The  $\chi_s^{(2)}$  term can therefore be neglected, and only  $\chi^{(3)'}$  needs to be considered in the model. Last, to account for long-range charge-charge correlations between different HA chains due to the weakly screened electrostatic field, we include the Debye-Hückel structure factor  $S_{\text{DH}}$  in the description of the scattering. Such a structure factor for overlapping hydration shells is known for electrolyte solutions (27) and is given by  $S_{\text{DH}}(q, \kappa) = q^2 / (q^2 + \kappa^2)$ . Taking these differences into account, we arrive at the following expression for  $S(\theta)$

$$S(\theta) = \frac{I(\theta)_{\text{PPP,HA}}}{I(\theta)_{\text{SSS,H}_2\text{O}}} = N_p \times |2 \Phi_0 (F_1(\theta, R) + F_3(\theta, R, \kappa)) \chi^{(3)' \cos(\theta/2)} (2 \cos(\theta) + 1) |^2 S_{\text{DH}}(q, \kappa) \quad (2)$$

where  $F_1 = 2\pi i R^2 \left( \frac{\sin(qR)}{(qR)^2} - \frac{\cos(qR)}{qR} \right)$  and  $F_3 = 2\pi i R^2 \frac{q \text{Rcos}(qR) + \kappa R \sin(qR)}{(qR)^2 + (\kappa R)^2}$  are scattering form factor functions (64). Equation 2 contains the following parameters:  $\Phi_0$ ,  $R$ ,  $\kappa$ , and  $\chi^{(3)'}$ . Of these,  $\kappa$  and  $\chi^{(3)'}$  are known and  $\Phi_0$  is independent of the HA concentration (64). The last parameter in the model is the effective size or radius  $R$ , defined here as the radial distance from which the electrostatic potential decays into the solution. This value is unknown. For a flexible charged polymer like HA in the dilute concentration range considered here,  $R$  must fall somewhere between the size of a completely collapsed chain and a fully extended one (69). Given that the intrachain electrostatic repulsion is the major contribution to the extension of the HA chain, we express  $R$  as a linear function of the Debye length, i.e.,  $R = \alpha \kappa^{-1}$ , where we will treat the proportionality constant  $\alpha$  as a fitting parameter to obtain  $R$ . Such a choice is in accordance with other size models, such as the Odijk-Skolnick-Fixman (OSF) theory (18, 19), although the exponent on  $\kappa^{-1}$  varies depending on the polyelectrolyte rigidity, the concentration regime, and the ionic strength (70, 71). We will discuss the general issue of polyelectrolyte size and the difference between  $R$  and the radius of gyration, as well as the difference in contrast mechanism further in the ‘‘Polyelectrolyte size: Comparing linear and nonlinear scattering’’ section.

To compare the model (Eq. 2) with the experimental data in Fig. 2 (B and C), we calculate the total fs-ESHS signal by numerically integrating the scattering pattern in the forward half-plane

$$S_{\text{int}} = \int_{-\pi/2}^{\pi/2} S(\theta) d\theta \quad (3)$$

The maximum scattering angle  $\theta_{\text{max}}$  of Fig. 2C can be obtained by computing the maximum of the scattering pattern in the forward half-plane, i.e., by differentiating and numerically solving for  $\theta$

$$\left. \frac{dS(\theta)}{d\theta} \right|_{\theta_{\max}} = 0 \quad (4)$$

The computed  $S_{\text{int}}$  and  $\theta_{\text{max}}$  values are shown in Fig. 2 (B and C) as solid lines. Using the single fit parameter  $\alpha$ , which takes a best-fit value of  $\alpha = 5$ , the curve for the total fs-ESHS intensity produced by this model (Fig. 2B) matches well with the measured values (circles), as well as the maximum scattering angle as a function of HA concentration (Fig. 2C). Considering that both the integrated intensity and the angle of maximum intensity are found with the same single fit parameter ( $\alpha$ ) suggests that our model captures the essentials of the fs-ESHS response.

### Concentration dependence

The modeling provides insight into the unusual concentration dependence of the fs-ESHS response of HA solutions. The initial rise in the intensity with HA concentration is due to the increasing number density of the number of HA chains and their extended hydration shells. At the same time, increasing the HA concentration adds counter-ions to the solution that increases the excess ionic strength and decreases the Debye screening length. This has three consequences: First, the HA chain collapses as the intrachain repulsion is weakened (reducing  $R$ ). Second, the extent of the hydration shells decreases because of increased Debye screening (reducing  $1/\kappa$  and  $R'$ ). Third, long-range charge-charge correlations between different HA chains are suppressed as well, reducing the structure factor. The peak integrated intensity at  $c_{\text{HA}} = 3.71$  nM ( $5 \mu\text{g/ml}$ ) is reached when the positive contribution from an increasing number density of HA starts to be outweighed by the opposing contributions from enhanced Debye screening. The increase in the scattering angle ( $\theta_{\text{max}}$ ) with HA concentration shown in Fig. 2C reflects the shrinking of both  $R$  and  $R'$ .

### Polyelectrolyte size: Comparing linear and nonlinear scattering

The size determined via fs-ESHS ( $R$ ) is related to the charge-induced water orientation: It can be considered as the radial distance where the average electrostatic potential experiences a maximum. This is a different metric than those used by more standard experimental methods to determine polyelectrolyte size, which rely on refractive index contrasts as experienced by light (dynamic light scattering), x-rays (small-angle x-ray diffraction), or neutrons (small-angle neutron scattering) (16, 17, 71). Besides the difference in contrast

mechanism, there is also a difference in sensitivity range: fs-ESHS works well at very low concentrations and ionic strengths  $\sim 3$  orders of magnitude below those of linear scattering, as it is very sensitive to the electrostatic field effects, whereas the linear light scattering methods perform well at high ionic strength and concentration. A direct comparison of experimental values of, for example, the radius of gyration ( $r_g$ ) with  $R$  in this study is therefore difficult. It could be done if there was a theoretical description that was valid for the entire range of concentrations, molar masses, and ionic strengths studied here and in the literature. Connecting  $R$  and  $r_g$  through a common theory, one would be able to connect both types of contrast mechanism. However, the most widely used model, OSF theory (18, 19), describes the polyelectrolyte size with a combination of thermal and electrostatic interactions. OSF theory is valid when  $a \ll \sqrt{\lambda_B L_0}$  (20), where  $a$  is the separation between the charges ( $a=1.02$  nm for HA),  $\lambda_B$  is the Bjerrum length ( $\lambda_B=0.71$  nm), and  $L_0$  is the intrinsic persistence length of HA [ $L_0=8$  nm; (17)]. For HA,  $\sqrt{\lambda_B L_0} = 2.4$  nm, meaning that the chain is assumed to be stiffer than it actually is. In addition, the relationship between a computed value such as the end-to-end distance ( $r_0$ ) and the experimentally measured radius of gyration is not well determined (72): For a neutral flexible chain, the ratio between  $r_0$  and  $r_g$  is  $\sqrt{6}$ , whereas for a stiff rod it is  $\sqrt{12}$ . Here, we take  $\sqrt{9} = 3$  as determined by (72), who found this value to be true for short HA chains (<64 monomers). Although there are  $\sim 3000$  monomers per chain in this study, we assume that the number of monomers does not influence this relation significantly.

Figure 4A presents a comparison of the variation of  $R$  (i.e., the size of the polymer as determined by the radial distance from which the electrostatic potential decays into the solution) and  $R'$  (i.e., the size of the polymer chain and the region with a nonnegligible electrostatic potential), together with the radius of gyration as determined by OSF theory from the end-to-end distance (17–19). The contour length  $L_c$  (i.e., the length at maximum extension) and the free radius per HA,  $R_{\text{free}}$ , are also plotted.  $R_{\text{free}}$  is calculated as follows:  $R_{\text{free}} = \left( \frac{3M_{\text{HA}}}{4\pi c_{\text{HA}} N_A} \right)^{1/3}$ , where  $M_{\text{HA}}$  is the average molar weight of HA ( $M_{\text{HA}}=1349$  kDa),  $N_A$  is Avogadro's constant, and  $c_{\text{HA}}$  is the HA concentration (in micrograms per milliliter). It can be seen that the contour length is larger than all other size parameters, where  $L_c$  represents the end-to-end distance of a fully stretched chain. The computed  $r_g$  is larger than both  $R$  and  $R'$  for the entire concentration

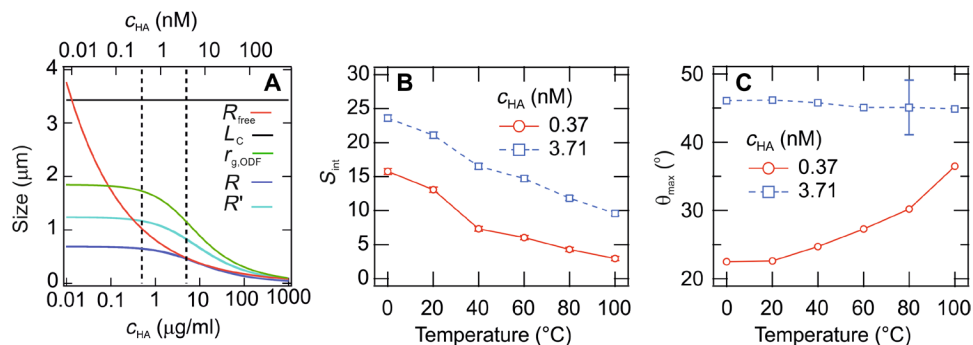


**Fig. 4. Relevant length scales as a function of HA concentration and the temperature dependence of the fs-ESHS response of HA in H<sub>2</sub>O.** (A) Comparison of measured sizes using fs-ESHS and values found from OSF theory, showing  $R$  and  $R'$  as a function of the concentration, together with the contour length  $L_c$ , the computed radius of gyration  $r_g$ , and the free radius per HA chain  $R_{\text{free}}$ . (B) Temperature dependence of total fs-ESHS intensity and (C) maximum scattering angle at HA concentrations (molecular weight, 1350 kDa) of  $0.5 \mu\text{g/ml}$  (red circles) and  $5 \mu\text{g/ml}$  (blue squares).

range. Because OSF theory is valid only for rigid polyelectrolytes such as DNA, i.e., when  $a \ll \sqrt{\lambda_B L_0}$  (20),  $r_g$  is likely overestimated. Furthermore, because the contrast mechanisms vary between linear and nonlinear scattering, making a direct comparison of size parameters is not possible. Thus, while the size determined by nonlinear light scattering is of the same order of magnitude compared to what could be found from linear light scattering measurement if the experiment were possible, due to the number of uncertainties, it is very difficult to make any more precise conclusions.

### Extended hydration shell

Last, we determine the extended hydration shell ( $R_h$ ) around the polyelectrolyte. The extended hydration shell is determined by the water that interacts with the HA chain and hence does not relate directly to  $R$  or  $R'$ . The maximum extended hydration shell that can be reached theoretically is determined by the available free volume per HA molecule. Figure 4A also shows the radius based on the available free volume (red line,  $R_{\text{free}}$ ). When  $R_{\text{free}} > R'$ , there is no interaction between the HA chains or soft shells [ $c_{\text{HA}} < 0.22$  nM (0.3  $\mu\text{g/ml}$ )]. When  $R_{\text{free}} < R'$ , we expect that the extended hydration shell will be in the range  $R < R_h < R'$ . At the concentration where the maximum intensity is reached, we expect that the extended hydration shell is maximum. To determine its magnitude, instead of using a model, we have performed fs-ESHS experiments at different temperatures, which allows us to vary the interaction strength of the HA chains and the water and thus determine whether  $R_{\text{free}} = R_h$ . Increasing the temperature increases the relative importance of random thermal motion compared to ion-water (charge-dipole) interactions. It also changes the screening length. With increasing temperature, the orientational order of water will reduce, and we expect that this will lead to a decrease in the integrated fs-ESHS intensity  $S_{\text{int}}$ . This intensity decrease arises from both a change in orientational order and a potential change in  $R$ , due to the altered dipole-charge interactions. If the effective size  $R$  decreases with temperature as well, we expect to see an increase in the scattering angle of maximum intensity  $\theta_{\text{max}}$ . However, if  $R$  is limited by the available free volume per HA chain ( $R_{\text{free}}$ ), we do not expect to see an additional change in  $\theta_{\text{max}}$ . In this case, the size of the hydration shell is equal to the radius of free volume per HA chain shown in Fig. 4A, i.e.,  $R_{\text{free}} = R_h$ .

Figure 4B shows the temperature dependence of the total fs-ESHS intensity measured between 0° and 100°C at two HA concentrations: 0.371 (0.5  $\mu\text{g/ml}$ ) and 3.71 nM (5  $\mu\text{g/ml}$ ), indicated by the dashed lines in Fig. 4A. As expected, the intensity decreases monotonically with temperature due to decreased orientational order. Note that the increase of temperature from 0° to 100°C also increases the Debye length by 20 nm at  $c_{\text{HA}} = 0.371$  nM (0.5  $\mu\text{g/ml}$ ) and by 15 nm at  $c_{\text{HA}} = 3.71$  nM (5  $\mu\text{g/ml}$ ), but this effect is not significant compared to the decrease in the orientational order from thermal motion. The maximum scattering angle  $\theta_{\text{max}}$  as a function of temperature for the two HA concentrations is plotted in Fig. 4C. At  $c_{\text{HA}} = 0.371$  nM (0.5  $\mu\text{g/ml}$ ), we observe a rise in  $\theta_{\text{max}}$  with temperature that reflects the shrinking of the extended hydration shell, and thus, the extended hydration shell is smaller than the free radius. However, at  $c_{\text{HA}} = 3.71$  nM (5  $\mu\text{g/ml}$ ),  $\theta_{\text{max}}$  is independent of temperature, indicating that the size of the hydration shell is constant. We therefore conclude that the theoretical extent of the hydration shells is at least equal to the free radius of HA at 3.71 nM, i.e.,  $R_h \geq R_{\text{free}}$ , amounting to an extended hydration shell with a radius of

$R_h = 475$  nm.  $R_h < R'$ , which means that although the electrostatic field is still orienting water molecules, these water molecules are not directly associated with the HA chain. Applying the same reasoning for  $\text{D}_2\text{O}$ , assuming that at the concentration of maximum intensity the free radius equals the radius of the extended hydration shell as for HA in  $\text{H}_2\text{O}$ , we estimate the size of the extended hydration shell in  $\text{D}_2\text{O}$  at 27 nM (32  $\mu\text{g/ml}$ ) to be 260 nm per HA or 45% of the value for  $\text{H}_2\text{O}$ .

A shell with a radius of 475 nm holds  $\sim 1.3 \times 10^{10}$  water molecules and one polymer chain, whose volume will displace only  $\sim 20,000$  water molecules. The measured value of  $R_h$  therefore reports on spatiotemporally averaged values. Compared to the value found for  $R$  (458 nm), which represents the radial position where the electrostatic potential changes, there is thus an additional shell of oriented water that is associated with the HA chain that has a thickness of 17 nm (37% of the Debye length at this concentration) or  $\sim 60$  water molecules in diameter. This number of hydrating water molecules that surround the charged HA polymer is similar to the number of  $\sim 77$  water molecules that were found around electrolytes in an earlier fs-ESHS study (27).

In summary, we have probed the extended hydration of HA, a biological anionic polyelectrolyte, using fs-ESHS. The source of the measured coherent second-harmonic radiation is assigned to water molecules that interact with the electrostatic field of spatially correlated charges on the polyelectrolyte chain. The fs-ESHS response is compared to dilute electrolyte solutions, which also display an increase in second-harmonic intensity at very low ionic strengths ( $\sim 10^{-5}$  M). Unlike for simple electrolyte solutions, the fs-ESHS intensity versus HA concentration curve displays a maximum at an intermediate concentration ( $\sim 13.3$   $\mu\text{g/ml}$ , 11.6 nM) that is 6 $\times$  larger than the intensity scattered by simple electrolytes. This difference is explained by the larger magnitude of the electrostatic field generated by HA compared to randomly distributed ions. At higher concentrations, the intensities scattered by HA and electrolyte solutions converge to the same plateau. This is explained by an enhancement of Debye screening with increasing HA concentration that results in a shrinkage of the hydration shells. A theoretical model that treats HA as a flexible charged particle surrounded by a spherical shell of polarized water molecules successfully describes the changes in the fs-ESHS intensity and angle as a function of HA concentration (ionic strength). Using this model, we propose a method to determine the size of polyelectrolyte hydrates in dilute solutions. Temperature-dependent fs-ESHS experiments were used to estimate the size of the extended hydration shell, which amounts to a few hundred nanometers for a concentration of 13.3  $\mu\text{g/ml}$  (11.6 nM). Similar to simple salt solutions, a clear difference between light and heavy water is observed. In heavy water, the fs-ESHS intensity maximum is 4.3 $\times$  lower and occurs at 2.4 $\times$  higher HA concentration (ionic strength). This difference cannot be explained by the proposed model and likely stems from the same nuclear quantum effect observed in simple electrolyte solutions (27). This isotope effect indicates that the interactions leading to the observed behavior not only are charge-water interactions but also contain interactions of the electrostatic field with the collective hydrogen bond network.

## MATERIALS AND METHODS

### Chemicals

HA (sodium hyaluronate, structure shown in Fig. 1A) produced by microbial fermentation of *Streptococcus pyogenes* was purchased

from R&D Systems (molecular weight, 1350 kDa) and Contipro a.s. (molecular weight, 1145 kDa) and used as received. The salts NaCl (Sigma-Aldrich; >99.999%) and MgCl<sub>2</sub> (Chempura; >99.995%) were filtered through Millipore Millex-VV 0.1- $\mu$ m polyvinylidene difluoride membrane filters. We used ultrapure water (>18.2 megohm-cm) dispensed from a Milli-Q UF-Plus instrument (Millipore Inc.). Ultrapure heavy water (D<sub>2</sub>O, 99.8% D) was purchased from Armar Chemicals. Stock solutions of HA were prepared by reconstituting a weighted amount of HA powder in water. Individual samples were prepared by diluting a stock solution of HA in new Eppendorf tubes. The tubes were cleaned before use by rinsing with water.

### Determination of the ionic strength at infinite dilution

The ionic strength at infinite dilution,  $I_0$ , was estimated from conductivity measurements with an HI 5522 pH/ISE/EC bench meter and HI 76312 conductivity electrode (Hanna Instruments) in combination with tabulated ionic molar conductivities (73) using the formula

$$I_0 = \frac{\kappa}{\sum_i \nu_i \lambda_i} \quad (5)$$

where  $\kappa$  is the specific conductance,  $\lambda_i$  is the equivalent ionic conductivities of the cations and anions, and  $\nu_i$  refers to the number of moles of cations and anions. To estimate  $I_0$ , we measured the ionic strength of pure water that was contained in the SHS cuvettes. On the basis of these conductivity measurements, we determined  $I_0 = (5.1 \pm 2.3) \times 10^{-6}$  M, assuming monovalent ions with  $\lambda_i \approx 60 \times 10^{-4}$  S m<sup>2</sup> mol<sup>-1</sup> (73).

### Angle-resolved second-harmonic scattering

The light source for fs-ESHS measurements was a Yb:KGW laser (Pharos SP, Light Conversion) producing 190-fs pulses centered at 1028 nm with a 200-kHz repetition rate. The polarization of the incident pulses was controlled via a Glan-Taylor polarizer (GT10-B, Thorlabs) and a zero-order half-wave plate (WPH05M-1030, Thorlabs). The incident laser pulses were filtered via a long-pass filter with a cutoff wavelength at 750 nm (FEL0750, Thorlabs). The average incident power at the sample was 60 mW (0.3  $\mu$ J per pulse). The laser beam was focused into a disposable cylindrical glass cuvette with an inner diameter of 4.2 mm (LS Instruments). The beam waist in the sample was 35  $\mu$ m at the focus with a Rayleigh length of 0.94 mm. SHS light at 514 nm was collected with a plano-convex lens ( $f = 50$  mm) and then filtered through a 10- or 50-nm-wide bandpass filter centered at 515 nm (ET515/10; ET515/50, Chroma). A Glan-Taylor polarizer (GT10-A, Thorlabs) was used for the polarization analysis of the scattered light. The polarization of the incident and outgoing light was either parallel (P) or perpendicular (S) with respect to the horizontal scattering plane. The SH light was focused using a plano-convex lens ( $f = 25$  mm) into a gated photo-multiplier tube (H7421-40, Hamamatsu). A more detailed description of the setup can be found in (74).

The experimental conditions used for fixed-angle measurements in Fig. 1 and figs. S2 and S4 were similar to those of (27, 48, 52). The detection angle was set to 90° with an acceptance angle of 11.4°. Each data point is an average of three to five measurements. Each measurement is an average of 50 exposures lasting 1 s each, i.e., using  $50 \times 2 \times 10^5$  pulses in total. The gate width was 10 ns. The fs-ESHS intensity at 90° was normalized by dividing the measured intensity of the sample solution by the intensity of the neat solvent (H<sub>2</sub>O or D<sub>2</sub>O) in the same polarization combination.

Angle-resolved fs-ESHS measurements shown in Figs. 2 and 4 and figs. S1 and S3 were performed by moving the detector arm in 5° steps between -90° and +90° with an opening angle of 3.4°. The normalized intensity at the angle  $\theta$ ,  $S(\theta)$ , was normalized to the intensity of the neat water (H<sub>2</sub>O or D<sub>2</sub>O) using the formula

$$S(\theta) = \frac{I(\theta)_{\text{PPP,sample}} - I(\theta)_{\text{PPP,water}}}{I(\theta)_{\text{SSS,water}}} \quad (6)$$

where PPP and SSS refer to the polarization combination of the incident and outgoing light [the first letter refers to the polarization state of the SH beam, and the second and third letters refer to that of the fundamental beam; P (S) is parallel (perpendicular) to the scattering plane]. The integrated fs-ESHS intensity was calculated by summing the normalized fs-ESHS intensity over all angles between -90° and 90° (except for 0°) using the formula

$$S_{\text{int}} = \sum_{\theta \neq 0} S(\theta) \quad (7)$$

### SUPPLEMENTARY MATERIALS

Supplementary material for this article is available at <http://advances.sciencemag.org/cgi/content/full/7/10/eabf2558/DC1>

[View/request a protocol for this paper from Bio-protocol.](#)

### REFERENCES AND NOTES

- M.-C. Bellissent-Funel, A. Hassanali, M. Havenith, R. Henchman, P. Pohl, F. Sterpone, D. van der Spoel, Y. Xu, A. E. Garcia, Water determines the structure and dynamics of proteins. *Chem. Rev.* **116**, 7673–7697 (2016).
- L. Zhang, L. Wang, Y.-T. Kao, W. Qiu, Y. Yang, O. Okobiah, D. Zhong, Mapping hydration dynamics around a protein surface. *Proc. Natl. Acad. Sci. U.S.A.* **104**, 18461–18466 (2007).
- Y. Levy, J. N. Onuchic, Water mediation in protein folding and molecular recognition. *Annu. Rev. Biophys. Biomol. Struct.* **35**, 389–415 (2006).
- W. H. Briscoe, S. Titmuss, F. Tiberg, R. K. Thomas, D. J. McGillivray, J. Klein, Boundary lubrication under water. *Nature* **444**, 191–194 (2006).
- M. K. Cowman, H. G. Lee, K. L. Schwertfeger, J. B. McCarthy, E. A. Turley, The content and size of hyaluronan in biological fluids and tissues. *Front. Immunol.* **6**, 261 (2015).
- J. Fraser, T. Laurent, U. Laurent, Hyaluronan: Its nature, distribution, functions and turnover. *J. Intern. Med.* **242**, 27–33 (1997).
- J. Seror, Y. Merkher, N. Kampf, L. Collinson, A. J. Day, A. Maroudas, J. Klein, Normal and shear interactions between hyaluronan–aggrecan complexes mimicking possible boundary lubricants in articular cartilage in synovial joints. *Biomacromolecules* **13**, 3823–3832 (2012).
- L. W. Moreland, Intra-articular hyaluronan (hyaluronic acid) and hylans for the treatment of osteoarthritis: Mechanisms of action. *Arthritis Res. Ther.* **5**, 54 (2003).
- A. Mráček, J. Varhaníková, M. Lehocký, L. Grundělová, A. Pokopcová, V. Velebný, The influence of Hofmeister series ions on hyaluronan swelling and viscosity. *Molecules* **13**, 1025–1034 (2008).
- A. Albersdörfer, E. Sackmann, Swelling behavior and viscoelasticity of ultrathin grafted hyaluronic acid films. *Eur. Phys. J. B* **10**, 663–672 (1999).
- C. B. Shah, S. M. Barnett, Swelling behavior of hyaluronic acid gels. *J. Appl. Polym. Sci.* **45**, 293–298 (1992).
- M. Cohen, E. Klein, B. Geiger, L. Addadi, Organization and adhesive properties of the hyaluronan pericellular coat of chondrocytes and epithelial cells. *Biophys. J.* **85**, 1996–2005 (2003).
- M. Cohen, D. Joester, I. Sabanay, L. Addadi, B. Geiger, Hyaluronan in the pericellular coat: An additional layer of complexity in early cell adhesion events. *Soft Matter* **3**, 327 (2007).
- M. Benz, N. Chen, J. Israelachvili, Lubrication and wear properties of grafted polyelectrolytes, hyaluronan and hylan, measured in the surface forces apparatus. *J. Biomed. Mater. Res. A* **71**, 6–15 (2004).
- J. Seror, Y. Merkher, N. Kampf, L. Collinson, A. J. Day, A. Maroudas, J. Klein, Articular cartilage proteoglycans as boundary lubricants: Structure and frictional interaction of surface-attached hyaluronan and hyaluronan–aggrecan complexes. *Biomacromolecules* **12**, 3432–3443 (2011).
- E. Buhler, F. Boué, Chain persistence length and structure in hyaluronan solutions: Ionic strength dependence for a model semirigid polyelectrolyte. *Macromolecules* **37**, 1600–1610 (2004).

17. E. Buhler, F. Boué, Persistence length for a model semirigid polyelectrolyte as seen by small angle neutron scattering: A relevant variation of the lower bound with ionic strength. *Eur. Phys. J. E* **10**, 89–92 (2003).
18. T. Odijk, Polyelectrolytes near the rod limit. *J. Polym. Sci. B Polym. Phys.* **15**, 477–483 (1977).
19. J. Skolnick, M. Fixman, Electrostatic persistence length of a wormlike polyelectrolyte. *Macromolecules* **10**, 944–948 (1977).
20. J.-L. Barrat, J.-F. Joanny, Persistence length of polyelectrolyte chains. *EPL* **24**, 333 (1993).
21. H. N. Joshi, E. M. Topp, Hydration in hyaluronic acid and its esters using differential scanning calorimetry. *Int. J. Pharm.* **80**, 213–225 (1992).
22. J. Liu, M. Cowman, Thermal analysis of semi-dilute hyaluronan solutions. *J. Therm. Anal. Calorim.* **59**, 547–557 (2000).
23. R. Servaty, J. Schiller, H. Binder, K. Arnold, Hydration of polymeric components of cartilage—An infrared spectroscopic study on hyaluronic acid and chondroitin sulfate. *Int. J. Biol. Macromol.* **28**, 121–127 (2001).
24. Y. Maréchal, M. Milas, M. Rinaudo, Hydration of hyaluronan polysaccharide observed by IR spectrometry. III. Structure and mechanism of hydration. *Biopolymers* **72**, 162–173 (2003).
25. J. Hunger, A. Bernecker, H. J. Bakker, M. Bonn, R. P. Richter, Hydration dynamics of hyaluronan and dextran. *Biophys. J.* **103**, L10–L12 (2012).
26. A. Davies, J. Gormally, E. Wyn-Jones, D. Wedlock, G. Phillips, A study of factors influencing hydration of sodium hyaluronate from compressibility and high-precision densimetric measurements. *Biochem. J.* **213**, 363–369 (1983).
27. Y. Chen, H. I. Okur, N. Gomopoulos, C. Macias-Romero, P. S. Cremer, P. B. Petersen, G. Tocci, D. M. Wilkins, C. Liang, M. Ceriotti, S. Roke, Electrolytes induce long-range orientational order and free energy changes in the H-bond network of bulk water. *Sci. Adv.* **2**, e1501891 (2016).
28. D. Laage, T. Elsaesser, J. T. Hynes, Water dynamics in the hydration shells of biomolecules. *Chem. Rev.* **117**, 10694–10725 (2017).
29. D. Laage, G. Stirnemann, F. Sterpone, R. Rey, J. T. Hynes, Reorientation and allied dynamics in water and aqueous solutions. *Annu. Rev. Phys. Chem.* **62**, 395–416 (2011).
30. H. Bakker, Structural dynamics of aqueous salt solutions. *Chem. Rev.* **108**, 1456–1473 (2008).
31. P. Jungwirth, D. Laage, Ion-induced long-range orientational correlations in water: Strong or weak, physiologically relevant or unimportant, and unique to water or not? *J. Phys. Chem. Lett.* **9**, 2056–2057 (2018).
32. H. I. Okur, Y. Chen, D. M. Wilkins, S. Roke, The Jones-Ray effect reinterpreted: Surface tension minima of low ionic strength electrolyte solutions are caused by electric field induced water-water correlations. *Chem. Phys. Lett.* **684**, 433–442 (2017).
33. D. Borgis, L. Belloni, M. Levesque, What does second harmonic scattering measure in diluted electrolytes? *J. Phys. Chem. Lett.* **9**, 3698–3702 (2018).
34. S. Funkner, G. Niehues, D. A. Schmidt, M. Heyden, G. Schwaab, K. M. Callahan, D. J. Tobias, M. Havenith, Watching the low-frequency motions in aqueous salt solutions: The terahertz vibrational signatures of hydrated ions. *J. Am. Chem. Soc.* **134**, 1030–1035 (2012).
35. R. Buchner, G. T. Hefter, P. M. May, Dielectric relaxation of aqueous NaCl solutions. *J. Phys. Chem. A* **103**, 1–9 (1999).
36. R. Mancinelli, A. Botti, F. Bruni, M. A. Ricci, A. K. Soper, Perturbation of water structure due to monovalent ions in solution. *Phys. Chem. Chem. Phys.* **9**, 2959–2967 (2007).
37. I. Howell, G. Neilson, Hydration in concentrated aqueous solution. *J. Phys. Condens. Matter* **8**, 4455 (1996).
38. A. W. Omta, M. F. Kropman, S. Woutersen, H. J. Bakker, Negligible effect of ions on the hydrogen-bond structure in liquid water. *Science* **301**, 347–349 (2003).
39. K. J. Tielrooij, N. Garcia-Araez, M. Bonn, H. J. Bakker, Cooperativity in ion hydration. *Science* **328**, 1006–1009 (2010).
40. J. D. Smith, R. J. Saykally, P. L. Geissler, The effects of dissolved halide anions on hydrogen bonding in liquid water. *J. Am. Chem. Soc.* **129**, 13847–13856 (2007).
41. G. Stirnemann, E. Wernersson, P. Jungwirth, D. Laage, Mechanisms of acceleration and retardation of water dynamics by ions. *J. Am. Chem. Soc.* **135**, 11824–11831 (2013).
42. E. Pluharova, P. Jungwirth, N. Matubayasi, O. Marsalek, Structure and dynamics of the hydration shell: Spatially decomposed time correlation approach. *J. Chem. Theory Comput.* **15**, 803–812 (2019).
43. D. M. Wilkins, D. E. Manolopoulos, S. Roke, M. Ceriotti, Communication: Mean-field theory of water-water correlations in electrolyte solutions. *J. Chem. Phys.* **146**, 181103 (2017).
44. J. Duboisset, P.-F. Brevet, Salt-induced long-to-short range orientational transition in water. *Phys. Rev. Lett.* **120**, 263001 (2018).
45. A. P. Gaiduk, G. Galli, Local and global effects of dissolved sodium chloride on the structure of water. *J. Phys. Chem. Lett.* **8**, 1496–1502 (2017).
46. L. Belloni, D. Borgis, M. Levesque, Screened coulombic orientational correlations in dilute aqueous electrolytes. *J. Phys. Chem. Lett.* **9**, 1985–1989 (2018).
47. S. Roke, G. Gonella, Nonlinear light scattering and spectroscopy of particles and droplets in liquids. *Annu. Rev. Phys. Chem.* **63**, 353–378 (2012).
48. Y. Chen, N. Dupertuis, H. I. Okur, S. Roke, Temperature dependence of water-water and ion-water correlations in bulk water and electrolyte solutions probed by femtosecond elastic second harmonic scattering. *J. Chem. Phys.* **148**, 222835 (2018).
49. H. I. Okur, C. I. Drexler, E. C. Tyrode, P. S. Cremer, S. Roke, The Jones-Ray effect is not caused by surface active impurities. *J. Phys. Chem. Lett.* **9**, 6739–6743 (2018).
50. J. Wyman Jr., E. Ingalls, The dielectric constant of deuterium oxide. *J. Am. Chem. Soc.* **60**, 1182–1184 (1938).
51. J. Dedic, H. I. Okur, S. Roke, Polyelectrolytes induce water-water correlations that result in dramatic viscosity changes and nuclear quantum effects. *Sci. Adv.* **5**, eaay1443 (2019).
52. Y. Chen, H. I. Okur, C. Liang, S. Roke, Orientational ordering of water in extended hydration shells of cations is ion-specific and is correlated directly with viscosity and hydration free energy. *Phys. Chem. Chem. Phys.* **19**, 24678–24688 (2017).
53. C. Liang, G. Tocci, D. M. Wilkins, A. Grisafi, S. Roke, M. Ceriotti, Solvent fluctuations and nuclear quantum effects modulate the molecular hyperpolarizability of water. *Phys. Rev. B* **96**, 041407 (2017).
54. G. Gonella, C. Lütgebaucks, A. G. F. de Beer, S. Roke, Second harmonic and sum-frequency generation from aqueous interfaces is modulated by interference. *J. Phys. Chem. C* **120**, 9165–9173 (2016).
55. A. G. F. de Beer, R. K. Campen, S. Roke, Separating surface structure and surface charge with second-harmonic and sum-frequency scattering. *Phys. Rev. B* **82**, 235431 (2010).
56. R. Bersohn, Y. H. Pao, H. L. Frisch, Double-quantum light scattering by molecules. *J. Chem. Phys.* **45**, 3184–3198 (1966).
57. J. I. Dadap, J. Shan, T. F. Heinz, Theory of optical second-harmonic generation from a sphere of centrosymmetric material: Small-particle limit. *J. Opt. Soc. Am. B* **21**, 1328 (2004).
58. A. G. de Beer, S. Roke, Nonlinear Mie theory for second-harmonic and sum-frequency scattering. *Phys. Rev. B* **79**, 155420 (2009).
59. J. I. Dadap, Optical second-harmonic scattering from cylindrical particles. *Phys. Rev. B* **78**, 205322 (2008).
60. A. G. de Beer, S. Roke, J. I. Dadap, Theory of optical second-harmonic and sum-frequency scattering from arbitrarily shaped particles. *J. Opt. Soc. Am. B* **28**, 1374–1384 (2011).
61. R. W. Boyd, *Nonlinear Optics* (Elsevier, 2008).
62. A. G. F. de Beer, S. Roke, Sum frequency generation scattering from the interface of an isotropic particle: Geometrical and chiral effects. *Phys. Rev. B* **75**, 245438 (2007).
63. S. Ong, X. Zhao, K. B. Eisenthal, Polarization of water molecules at a charged interface: Second harmonic studies of the silica/water interface. *Chem. Phys. Lett.* **191**, 327–335 (1992).
64. C. Lütgebaucks, G. Gonella, S. Roke, Optical label-free and model-free probe of the surface potential of nanoscale and microscopic objects in aqueous solution. *Phys. Rev. B* **94**, 195410 (2016).
65. S. Roke, W. G. Roeterdink, J. E. G. J. Wijnhoven, A. V. Petukhov, A. W. Kleyn, M. Bonn, Vibrational sum frequency scattering from a submicron suspension. *Phys. Rev. Lett.* **91**, 258302 (2003).
66. A. Marchioro, M. Bischoff, C. Lütgebaucks, D. Biriukov, M. Předota, S. Roke, Surface characterization of colloidal silica nanoparticles by second harmonic scattering: Quantifying the surface potential and interfacial water order. *J. Phys. Chem. C* **123**, 20393–20404 (2019).
67. M. Bischoff, D. Biriukov, M. Předota, S. Roke, A. Marchioro, Surface potential and interfacial water order at the amorphous TiO<sub>2</sub> nanoparticle/aqueous interface. *J. Phys. Chem. C* **124**, 10961–10974 (2020).
68. G. S. Manning, Limiting laws and counterion condensation in polyelectrolyte solutions I. Colligative properties. *J. Chem. Phys.* **51**, 924 (1969).
69. P.-G. De Gennes, P. Pincus, R. M. Velasco, F. Brochard, Remarks on polyelectrolyte conformation. *J. Phys.* **37**, 1461–1473 (1976).
70. M. Le Bret, Electrostatic contribution to the persistence length of a polyelectrolyte. *J. Chem. Phys.* **76**, 6243 (1982).
71. V. Degiorgio, T. Bellini, F. Mantegazza, Measurements of the persistence length of flexible polyelectrolytes. *Int. J. Polym. Anal. Charact.* **2**, 83–93 (1995).
72. M. J. Stevens, K. Kremer, The nature of flexible linear polyelectrolytes in salt free solution: A molecular dynamics study. *J. Chem. Phys.* **103**, 1669–1690 (1995).
73. D. R. Lide, *CRC Handbook of Chemistry and Physics* (CRC Press, 2004).
74. N. Gomopoulos, C. Lütgebaucks, Q. Sun, C. Macias-Romero, S. Roke, Label-free second harmonic and hyper Rayleigh scattering with high efficiency. *Opt. Express* **21**, 815–821 (2013).
75. E. Fouissac, M. Milas, M. Rinaudo, R. Borsali, Influence of the ionic strength on the dimensions of sodium hyaluronate. *Macromolecules* **21**, 5613–5617 (1992).

#### Acknowledgments

**Funding:** This work is supported by the Julia Jacobi Foundation, the EPFL-WIS fund, and the European Research Council (grant number 616305). H.I.O. thanks EU MSCA-IF (Grant No. 899088) for financial support. **Author contributions:** J.D. performed the experiments. J.D.,

H.I.O., and S.R. interpreted the data and wrote the manuscript. S.R. conceived and supervised the work. The supporting material contains the following: fig. S1, power dependence of the fs-ESHS response; fig. S2, spectral recording of the fs-ESHS response; fig. S3, second-harmonic scattering patterns for HA (molecular weight, 1349 kDa) at various concentrations; fig. S4, normalized second-harmonic scattering intensity measured at a fixed angle of 90° with SSS polarization combination; fig. S5, fs-ESHS response from HA solutions at constant HA concentration as a function of excess ionic strength from added salt; fig. S6:  $S_{int}$  and  $\theta_{max}$  for other polyelectrolytes as well as a neutral polymer; table S1, experimental size studies in the literature of HA in aqueous solution. **Competing interests:** The authors declare that they have no competing interests. **Data and materials availability:** All data needed to evaluate the

conclusions in the paper are present in the paper and/or the Supplementary Materials. Additional data related to this paper may be requested from the authors.

Submitted 14 October 2020

Accepted 14 January 2021

Published 3 March 2021

10.1126/sciadv.abf2558

**Citation:** J. Dedic, H. I. Okur, S. Roke, Hyaluronan orders water molecules in its nanoscale extended hydration shells. *Sci. Adv.* **7**, eabf2558 (2021).

## Hyaluronan orders water molecules in its nanoscale extended hydration shells

J. Dedic, H. I. Okur and S. Roke

*Sci Adv* 7 (10), eabf2558.  
DOI: 10.1126/sciadv.abf2558

### ARTICLE TOOLS

<http://advances.sciencemag.org/content/7/10/eabf2558>

### SUPPLEMENTARY MATERIALS

<http://advances.sciencemag.org/content/suppl/2021/03/01/7.10.eabf2558.DC1>

### REFERENCES

This article cites 73 articles, 6 of which you can access for free  
<http://advances.sciencemag.org/content/7/10/eabf2558#BIBL>

### PERMISSIONS

<http://www.sciencemag.org/help/reprints-and-permissions>

Use of this article is subject to the [Terms of Service](#)

---

*Science Advances* (ISSN 2375-2548) is published by the American Association for the Advancement of Science, 1200 New York Avenue NW, Washington, DC 20005. The title *Science Advances* is a registered trademark of AAAS.

Copyright © 2021 The Authors, some rights reserved; exclusive licensee American Association for the Advancement of Science. No claim to original U.S. Government Works. Distributed under a Creative Commons Attribution NonCommercial License 4.0 (CC BY-NC).